Negative Differential Mobility and Trapping in Active Matter Systems

C. Reichhardt and C. J. O. Reichhardt

Theoretical Division and Center for Nonlinear Studies, Los Alamos National Laboratory, Los Alamos, New Mexico 87545, USA

E-mail: cjrx@lanl.gov

Abstract. Using simulations, we examine the average velocity as a function of applied drift force for active matter particles moving through a random obstacle array. We find that for low drift force, there is an initial flow regime where the mobility increases linearly with drive, while for higher drift forces a regime of negative differential mobility appears in which the velocity decreases with increasing drive due to the trapping of active particles behind obstacles. A fully clogged regime exists at very high drift forces when all the particles are permanently trapped behind obstacles. We find for increasing activity that the overall mobility is nonmonotonic, with an enhancement of the mobility for small levels of activity and a decrease in mobility for large activity levels. We show how these effects evolve as a function of disk and obstacle density, active run length, drift force, and motor force.

1. Introduction

There has been increasing interest in self-driven or active matter systems, which are often modeled as a collection of self-mobile disks with mobility represented by driven diffusion or run-and-tumble dynamics [1, 2]. When disk-disk interactions are included, an activity-induced clustering or phase separation into a dense solid phase coexisting with a low density active gas phase can occur for sufficiently high activity and disk density. Such clustering effects occur for both driven diffusive [3, 4, 5, 6, 7, 8] and run-and-tumble systems [3, 7, 8, 9]. Studies of active matter systems generally focus on samples with featureless substrates, but recent work has addressed the behavior of active matter interacting with more complex environments [2], such as random [10, 11, 12] or periodic obstacle arrays [13, 14, 15], pinning arrays or rough landscape substrates [15, 16, 17], or funnel arrays [18], as well as mixtures of active and passive particles [19]. In run-and-tumble disk systems, studies of the average flux through an obstacle array in the presence of an additional external drift force [10] show that for low activity or short run times, the active disks have Brownian characteristics and are easily trapped; however, for increasing run persistence length or activity, the trapping is reduced and the flux of disks through the system increases. Interestingly, when the run time or activity is large, the disk drift mobility is strongly reduced due to enhanced self-trapping of disks behind the obstacles and by each other. Other studies of active particles moving through an array of obstacles show that for increasing propulsion speed, the particles remain trapped behind obstacles for a longer time, and as a result the long time diffusion constant is decreased for high activity particles compared to passive or Brownian particles [12]. If the obstacles are replaced by a rough substrate, another study showed that the drift mobility of the particles increases with increasing run length since the self-clustering effect allows the particles to act like an effective larger-scale rigid object that couples only weakly to the substrate [17]. Studies of flocking active particles moving through obstacle arrays reveal nonmonotonic behavior as a function of disorder strength [20] and a disorder-induced flocking to non-flocking transition [11, 21].

Here we examine run-and-tumble active matter disks in the presence of a random array of obstacles where we apply an external driving force in order to measure the long time average disk drift velocity in the direction of drive. While in previous work we considered a constant applied drift force [10], here we examine the effects of varied drift forces and compare the resulting velocity-force curves to those found in other systems that exhibit depinning, such as passive particles driven over random disorder [22]. Previous studies of passive or Brownian particles driven though an obstacle array showed that there can be a regime of negative differential mobility where the velocity *decreases* with increasing drive, and the velocity can even drop to zero in the limit of large drive [23, 24, 25]. Negative differential mobility also appears when the obstacles themselves are allowed to move [26, 27, 28]. Such effects can arise for driven particles in laminar flows [29], particles driven through glass formers [30], vortices in type-II superconductors moving through periodic pinning arrays[22, 31, 32], colloids moving on ordered pinning arrays [33], and in nonequilibrium states of certain types of semiconductors [34].

We specifically examine run-and-tumble driven disks, where a motor force $F_m^i\hat{\mathbf{m}}$ acts on disk i during a fixed running time τ in a randomly chosen direction $\hat{\mathbf{m}}$. At the end of the running time, a new run begins with the motor force acting in a new randomly chosen direction. The disks move through a random array of obstacles

under an external drive $F_D\hat{\mathbf{x}}$, and we measure the average disk drift velocity $\langle V\rangle$ in the driving direction as a function of increasing F_D. At low drives $F_D \ll F_M$, the drift velocity $\langle V\rangle$ increases linearly with increasing F_D, but we find that $\langle V\rangle$ reaches a maximum and then decreases with increasing F_D due to the partial trapping of disks behind obstacles. For large enough drives $F_D > F_{cl}$ we observe a fully clogged state with $\langle V\rangle = 0$. The value of F_{cl} increases with increasing activity and saturates for long run times, while the maximum value of $\langle V\rangle$ changes nonmonotonically as a function of run time. In some cases, a system with longer run times has lower mobility for small F_D but higher mobility at large F_D compared to a system with shorter run times. For fixed run time and increasing motor force F_m, we find that the transition from a linear dependence of $\langle V\rangle$ on F_m to a decrease in $\langle V\rangle$ with increasing F_m follows the line $F_m = F_D$. When we increase the disk density, we observe crowding effects that reduce the overall mobility but can also increase the range of parameters for which negative differential mobility occurs.

2. Simulation

We consider a two-dimensional system of size $L \times L$ with periodic boundary conditions in the x and y directions, where $L = 50$. Within the system we place N_a active disks of radius $R = 0.5$ and $N_{\rm obs}$ obstacles which are modeled as stationary disks of the same size as the active disks. The area coverage of the obstacles is $\phi_{\rm obs} = N_{\rm obs}\pi R^2/L^2$, the area coverage of the active disks is $\phi_a = N_a\pi R^2/L^2$, and the total area coverage is $\phi_{\rm tot} = \phi_{\rm obs} + \phi_a$. The disk-disk interactions are modeled as a short range harmonic repulsion $\mathbf{F}_{dd} = k(d - 2R)\Theta(d - 2R)\hat{\mathbf{d}}$ where d is the distance between the disks, $\hat{\mathbf{d}}$ is the displacement vector between the disks, k is the spring constant, and Θ is the Heaviside step function. The dynamics of an active disk i are governed by the following overdamped equation of motion: $\eta d\mathbf{r}_i/dt = \mathbf{F}^i_{aa} + \mathbf{F}^i_m + \mathbf{F}^i_{\rm obs} + \mathbf{F}_D$ where the damping constant $\eta = 1.0$. Here $\mathbf{F}^i_{aa} = \sum_{j\neq i}^{N_a} F^{ij}_{dd}$ is the interaction between active disks and $\mathbf{F}^i_{\rm obs} = \sum_k^{N_{\rm obs}} F^{ik}_{dd}$ is the interaction between active disk i and the obstacles. Each mobile disk has a motor force $\mathbf{F}^i_m = F_m\hat{\mathbf{m}}^i$ applied in a randomly chosen direction $\hat{\mathbf{m}}^i$ which changes after each run time τ. In the absence of any collisions, during a running time the motor force translates the disk a distance $l_r = F_m\tau\delta t$, where $\delta t = 0.002$ is the simulation time step. The mobile disks experience an additional external driving force in the x direction, $\mathbf{F}_D = F_D\hat{\mathbf{x}}$. After changing F_D, we wait for at least 10^8 simulation time steps to ensure that we have reached a steady state flux before measuring the average drift velocity in the direction of drive, $\langle V\rangle = N_a^{-1}\sum_i^{N_a}\langle \mathbf{v}\cdot\hat{\mathbf{x}}\rangle_i$. We quantify the activity level of the disks in terms of l_r and F_m.

3. Results

In Fig. 1(a) we plot $\langle V\rangle$ versus F_D for a system with $F_m = 0.5$, $\phi_{\rm obs} = 0.1257$, and $l_r = 0.1$ at $\phi_a = 0.00785$, 0.03146, 0.0628, and 0.1257, and in Fig. 1(b) we show the same data on a log-log scale. At the low density of $\phi_a = 0.00785$, the sample behavior falls in the single active disk limit and $\langle V\rangle$ increases linearly with F_D before reaching a maximum near $F_D = 0.03$ and then decreasing to $\langle V\rangle = 0.0$ for $F_D \geq 0.21$. For $\phi_a = 0.03146$, $\langle V\rangle$ reaches a maximum near $F_D = 0.3$ and drops to zero for $F_D \geq 0.71$. In both cases the system exhibits what is called negative differential mobility (NDM), where the average velocity decreases with increasing F_D, and at high enough drives

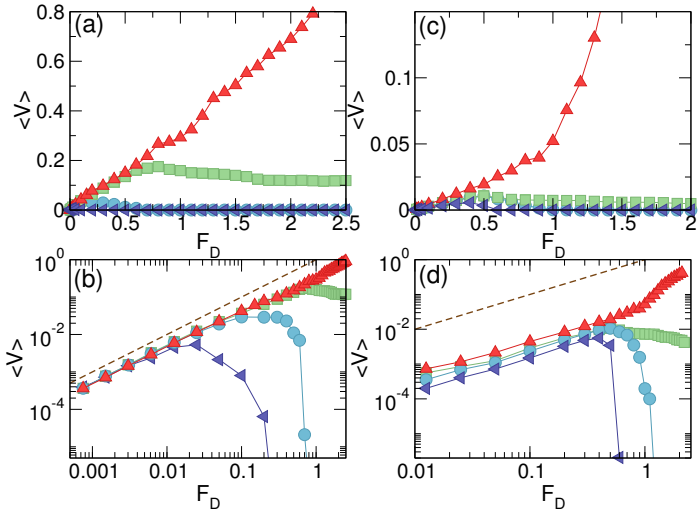

Figure 1. Average drift velocity $\langle V\rangle$ vs F_D in samples with $\phi_{\rm obs} = 0.1257$ and $F_m = 0.5$ for $\phi_a = 0.00785$ (dark blue left triangles), 0.03146 (light blue circles), 0.0628 (green squares), and 0.1257 (red up triangles). (a) $l_r = 0.01$. (b) Data from (a) on a log-log scale highlighting the negative differential mobility for $\phi = 0.00785$, 0.03146, and 0.0628. (c) $l_r = 120$. (d) Data from (c) on a log-log scale. The dashed lines in panels (b) and (d) indicate the linear behavior $\langle V\rangle = F_D$ in an obstacle-free system.

the sample reaches a pinned or clogged state. For $\phi = 0.0628$ there is still a region of NDM for $F_D > 0.8$; however, the velocity remains finite up to the maximum drive $F_D/F_m = 5$ that we consider. For $\phi = 0.1257$, when the number of disks equals the number of obstacles, the velocity monotonically increases with F_D and the NDM is lost. In Fig. 1(b) the dashed line indicates the linear behavior $\langle V\rangle = F_D$ of an obstacle-free system. For all values of ϕ_a, we find the same linear increase of $\langle V\rangle$ with F_D for small F_D, and the value of F_D at which NDM appears shifts to higher values of F_D as ϕ_a increases.

In Fig. 2 we show the trajectories of the active disks at three different values of F_D for the $\phi_a = 0.03146$ system from Fig. 1(a,b). At $F_D = 0.0125$ in Fig. 2(a), $\langle V\rangle$ is increasing with increasing F_D. The disk trajectories are space filling, and $F_D/F_m = 0.025$ is small enough that when a disk becomes trapped behind an obstacle, the motor force is large enough to move the disk in the direction opposite to the drive, permitting the disk to work its way around the obstacle. As a result, the active disks can easily explore nearly all the possible paths through the obstacle array. As F_D increases, the ability of the disks to back away from an obstacle is reduced, and the amount of time disks spend trapped behind obstacles increases, as illustrated in Fig. 2(b) at $F_D = 0.6$, corresponding to $F_D/F_m = 1.2$, where the system exhibits NDM. Here there are several locations in which the disks become trapped for long periods of time. As F_D is further increased, more disks become trapped and $\langle V\rangle$ diminishes, as shown in Fig. 2(c) for $F_D = 1.0$, where all the active disks are permanently trapped and $\langle V\rangle = 0$. Two effects reduce the trapping susceptibility as ϕ_a increases. Once a portion of the disks becomes trapped behind the most confining obstacle configurations, additional active disks can no longer be trapped at these same locations, meaning that the "deepest" traps are effectively inactivated. In addition,

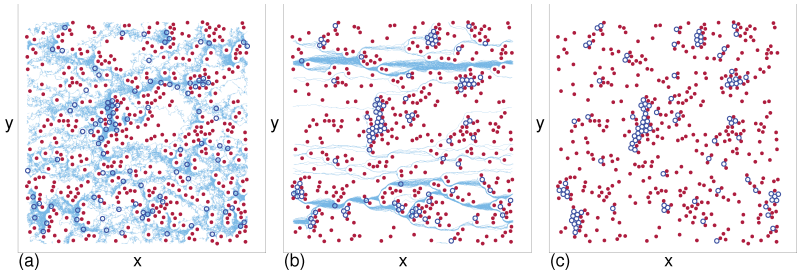

Figure 2. The obstacle positions (red filled circles), active disks (dark blue open circles), and trajectories (light blue lines) for the system from Fig. 1(a,b) with $\phi_{\rm obs} = 0.1257$, $\phi_a = 0.03146$, and $l_r = 0.01$. (a) $F_D = 0.0125$, where $\langle V \rangle$ is increasing with increasing F_D. (b) $F_D = 0.6$, where partial trapping of active disks behind the obstacles occurs and the system exhibits negative differential mobility. (c) $F_D = 1.0$, where $\langle V \rangle = 0$ and the system is in a completely clogged state.

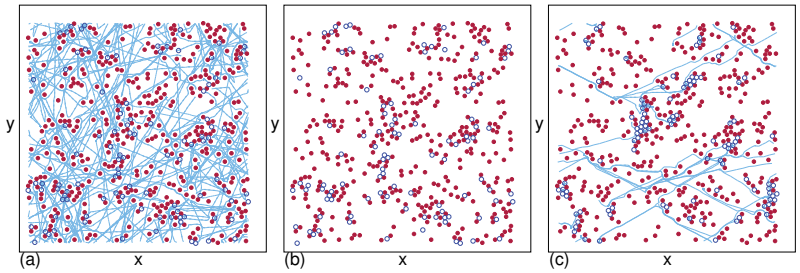

Figure 3. The obstacle positions (red filed circles), active disks (dark blue open circles), and trajectories (light blue lines) for the system in Fig. 1(c,d) with $\phi_{\rm obs} = 0.1257$, $\phi_a = 0.03146$, and $l_r = 120$. (a) $F_D = 0.0125$, where the disks move in straight lines. (b) The same as in (a) but without the trajectories, showing that nearly all of the active disks are in contact with an obstacle. (c) $F_D = 1.0$, where there is increased trapping but $\langle V \rangle$ remains finite, unlike the $l_r = 0.01$ case illustrated in Fig. 2(c) where complete trapping occurs.

at locations where N multiple active disks are trapped one behind another, there is a finite probability that the motor forces of these disks will simultaneously be oriented in the direction opposite to that of the drift force, permitting the disks to escape, so that complete trapping will occur only when $F_D > NF_m$.

In Fig. 1(c,d) we plot $\langle V \rangle$ versus F_D for the same system in Fig. 1(a,b) but with a much larger run length of $l_r = 120$. We observe the same general features as in the $l_d = 0.01$ case; however, the value of F_D at which $\langle V \rangle$ reaches zero is shifted upward and the magnitude of $\langle V \rangle$ for a given F_D is significantly reduced, as indicated by comparing the curves in Fig. 1(d) to the dashed line which is the flow expected in an obstacle-free system.

Figure 3(a) shows the active disk trajectories for the system in Fig. 1(c,d) with $\phi_a = 0.03146$ and $l_r = 120$ at $F_D = 0.0125$. In this regime, $\langle V \rangle$ is increasing with increasing F_D; however, $\langle V \rangle$ is smaller by nearly a factor of 20 than in the $l_r = 0.01$ case illustrated in Fig. 2(a). The active disks in Fig. 3(a) are not strongly affected by the external drive and move in straight lines while running; however, upon encountering an obstacle the active disk pushes against it and becomes self-trapped,

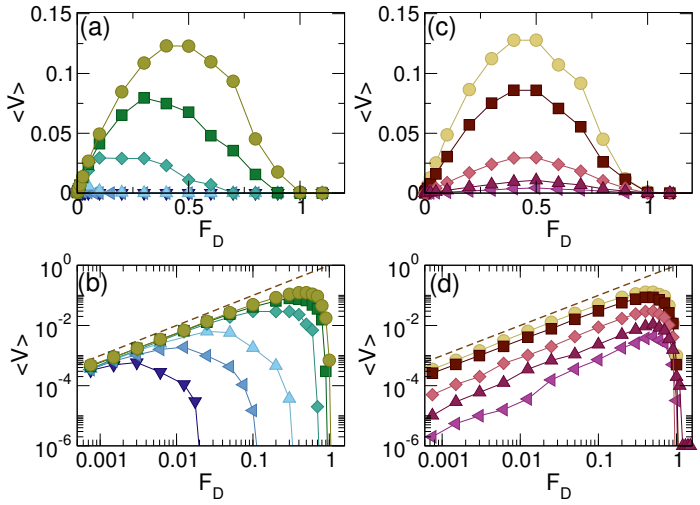

Figure 4. $\langle V\rangle$ vs F_D in samples with $\phi_{\rm obs} = 0.1257$, $F_m = 0.5$, and $\phi_a = 0.03146$. (a) $l_r = 0.002$ (dark blue down triangles), 0.01 (medium blue right triangles), 0.02 (light blue up triangles), 0.1 (teal diamonds), 0.3 (dark green squares), and 1.0 (light green circles), from bottom to top. (b) The curves from panel (a) plotted on a log-log scale. The dashed line indicates the obstacle-free limit of $\langle V\rangle = F_D$. Here $\langle V\rangle$ increases with increasing l_r. (c) $\langle V\rangle$ vs F_D for the same system with $l_r = 3$ (yellow circles), 10 (dark red squares), 40 (light pink diamonds), 120 (dark pink up triangles), and 320 (magenta triangles), from top to bottom. (d) The curves from panel (a) plotted on a log-log scale. The dashed line indicates the obstacle-free limit of $\langle V\rangle = F_D$. Here $\langle V\rangle$ decreases with increasing l_r.

reducing the mobility of the system. To more clearly demonstrate the self-trapping effect that occurs for large run lengths, in Fig. 3(b) we plot the same snapshot of the active disk and obstacle positions without trajectories, and find that nearly all of the active disks are in contact with an obstacle. At $F_D = 1.0$, as illustrated in Fig. 3(c), $\langle V\rangle$ is finite in the $l_r = 120$ system, whereas $\langle V\rangle = 0$ for $l_r = 0.01$. Here, although a considerable amount of disk trapping occurs, the longer run times allow some of the disks to become mobile, giving a nonzero contribution to $\langle V\rangle$.

To get a better understanding of how l_r affects the shape of the velocity-force curves, in Fig. 4(a) we plot $\langle V\rangle$ versus F_D for a sample with $\phi_{\rm obs} = 0.1257$, $\phi_a = 0.03146$, and $F_m = 0.5$ at l_r values ranging from $l_r = 0.002$ to $l_r = 1.0$. The same curves are shown on a log-log scale in Fig. 4(b), where the dashed line indicates the obstacle-free limit $\langle V\rangle = F_D$. We note that for non-active disks with $l_r = 0$, $\langle V\rangle = 0$ for all drive values at this disk density. Three trends emerge from the data. There is an overall increase in $\langle V\rangle$ with increasing l_r for all values of F_D. Additionally, both the maximum value of $\langle V\rangle$ and the drive at which $\langle V\rangle$ reaches zero shift to higher values of F_D with increasing l_r. Figure 4(c) shows $\langle V\rangle$ versus F_D in the same sample for l_r values ranging from $l_r = 3$ to $l_r = 320$, and in Fig. 4(d) we plot the same curves on a log-log scale. Here there is an overall decrease in $\langle V\rangle$ with increasing l_r for all values of F_D. The drive at which $\langle V\rangle$ reaches zero has its largest value of $F_D = 1.0$ for $l_r = 1.0$ and decreases with increasing l_r for $l_r > 1.0$. In the limit $l_r \to \infty$, $\langle V\rangle = 0$ for all F_D since fluctuations in the disk motion are eliminated, so the system cannot escape from a clogged state. This is similar to what occurs in the $l_r = 0$ nonactive

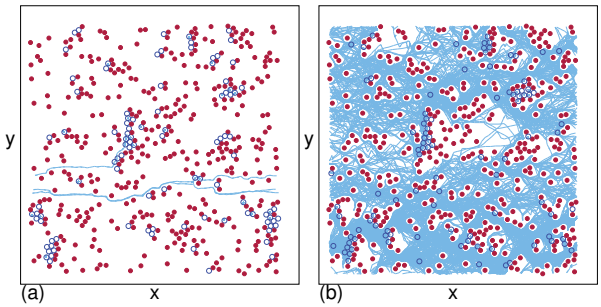

Figure 5. The obstacle positions (red filled circles), active disks (dark blue open circles), and trajectories (light blue lines) for the system in Fig. 4(a) at $\phi_{\rm obs} = 0.1257$, $F_m = 0.5$, $\phi_a = 0.03146$, and $F_D = 0.5$. (a) At $l_r = 0.02$, most disks are trapped. (b) At $l_r = 3.0$, the flow through the sample is optimized.

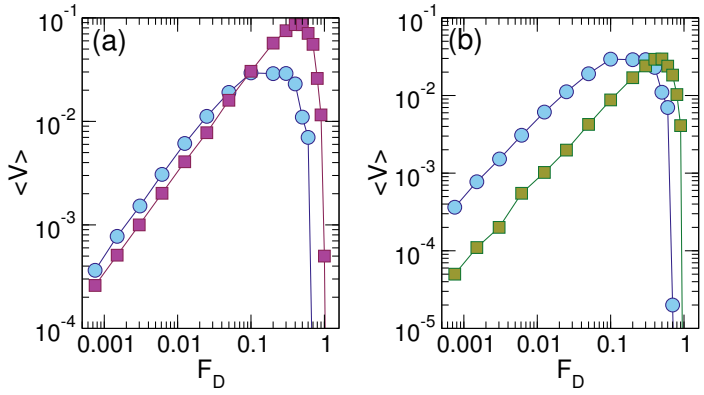

Figure 6. The drift velocity $\langle V \rangle$ vs F_D for the system in Fig. 3 with $\phi_{\rm obs} = 0.1257$, $F_m = 0.5$, and $\phi_a = 0.03146$. (a) $l_r = 0.1$ (blue circles) and $l_r = 10$ (magenta squares). (b) $l_r = 0.1$ (blue circles) and $l_r = 40$ (green squares). In both cases there is a crossing of the curves.

disk system.

In Fig. 5(a) we illustrate the active disk trajectories for the system in Fig. 4 at $F_D = 0.5$ for $l_r = 0.02$, where most of the disks are trapped. At later times, all the disks become trapped and $\langle V \rangle = 0$. In Fig. 5(b) we show the same system at $l_r = 3.0$ and $F_D = 0.5$, where $\langle V \rangle$ passes through its maximum value in Fig. 4(c,d). Here the disks can move easily through the system and the amount of trapping is significantly reduced. At higher values of F_D more trapping occurs, and for large enough F_D, $\langle V \rangle = 0$.

The value of l_r that maximizes the flux through the system depends strongly on F_D. In Fig. 6(a) we plot $\langle V \rangle$ versus F_D for the system in Fig. 4 at $l_r = 0.1$ and $l_r = 10$. For $F_D < 0.1$, $\langle V \rangle$ is larger in the $l_r = 0.1$ system than in the $l_r = 10$ system, while for $F_D > 0.1$, the situation is reversed and $\langle V \rangle$ is largest in the $l_r = 10$ system. A comparison of $\langle V \rangle$ versus F_D for $l_r = 0.1$ and $l_r = 40$ appears in Fig. 6(b), where $\langle V \rangle$ is larger in the $l_r = 0.1$ system for $F_D < 0.3$ and larger in the $l_r = 40$ system for $F_D > 0.3$, while the maximum value of $\langle V \rangle$ is nearly the same for both values of l_r. This result has implications for active particle separation or mixing, and indicates that

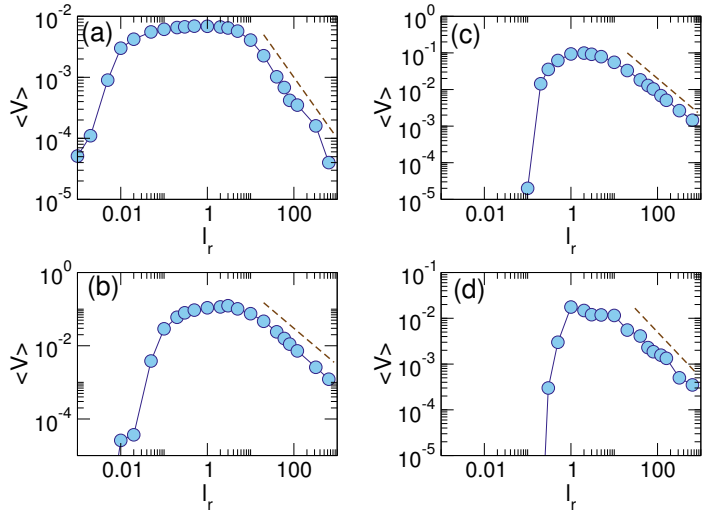

Figure 7. $\langle V\rangle$ vs l_r for samples with $\phi_{\rm obs} = 0.1257$, $F_m = 0.5$, and $\phi_a = 0.03146$. (a) $F_D = 0.0125$. (b) $F_D = 0.3$. (c) $F_D = 0.7$. (d) $F_D = 0.9$. Dashed lines indicate fits to $\langle V\rangle \propto l_r^{-1}$

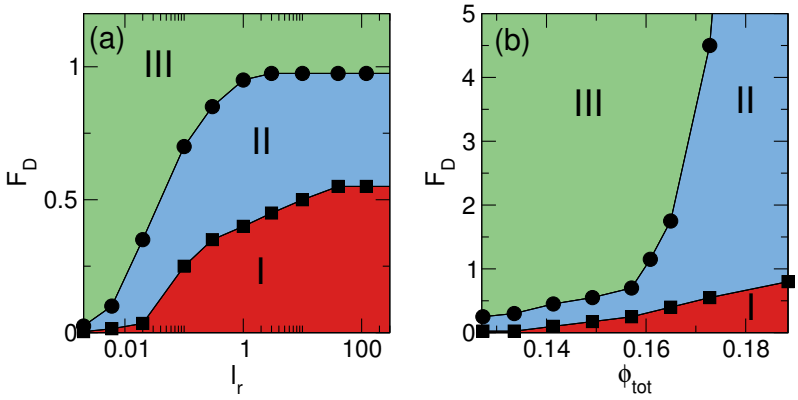

Figure 8. Dynamic phase diagrams. Phase I (red) is the ohmic flow regime in which $\langle V\rangle$ increases with increasing F_D. Phase II (blue) is the partial trapping regime where NDM occurs. Phase III (green) is the complete clogging regime in which $\langle V\rangle = 0$. (a) Dynamic phase diagram as a function of F_D vs l_r for a system with $\phi_{\rm obs} = 0.1257$, $\phi_a = 0.03146$, and $F_m = 0.5$. (b) Dynamic phase diagram as a function of F_D vs $\phi_{\rm tot}$ for $\phi_{\rm obs} = 0.1257$ and $F_m = 0.5$.

a less active particle species would move faster under a drift force at smaller F_D than a more active particle species. At larger F_D the reverse would occur, with the less active species becoming immobile while the more active particles are still able to flow through the system. The curves in Fig. 6 also indicate that is possible to tune F_D such that active particle species with very different activity levels drift with equal values of $\langle V\rangle$, such as by setting $F_D = 0.3$ for the $l_r = 0.1$ and $l_r = 40$ disks in Fig. 6(b). It is possible that certain living systems such as bacteria subjected to an external drift may actually lower their activity in order to move through a heterogeneous environment if the external flow is weak, while if there is a strong drift flow, an increase in the

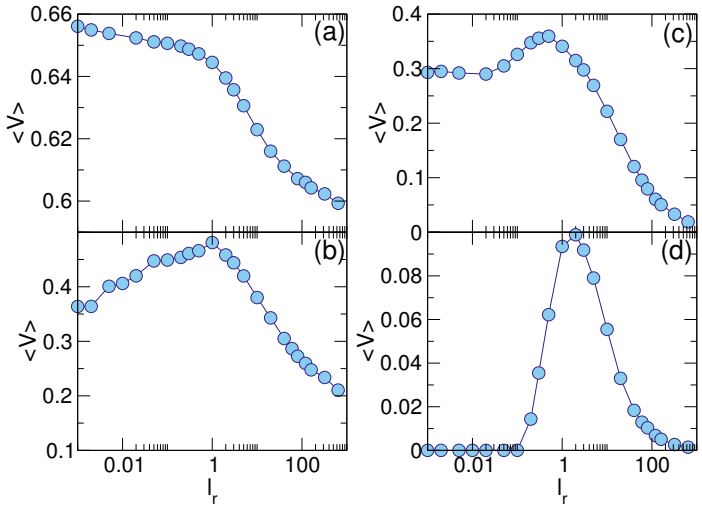

Figure 9. $\langle V\rangle$ vs l_r for samples with fixed $\phi_{\rm tot} = 0.157$ and varied $\phi_{\rm obs}$. (a) $\phi_{\rm obs} = 0.03146$. (b) $\phi_{\rm obs} = 0.0628$. (c) $\phi_{\rm obs} = 0.09424$. (d) $\phi_{\rm obs} = 0.1257$.

activity level would improve the mobility.

In Fig. 7 we plot $\langle V\rangle$ versus l_r for the system in Fig. 1 with $\phi_{\rm obs} = 0.1257$, $F_m = 0.5$, and $\phi_a = 0.03146$ for different values of F_D. For $F_D = 0.0125$ in Fig. 7(a), $\langle V\rangle$ initially increases with increasing l_r before reaching a maximum value at $l_r = 1.0$, after which it drops by several orders of magnitude as $l_r \to 320$. At $F_D = 0.3$ in Fig. 7(b), $F_D = 0.7$ in Fig. 7(c), and $F_D = 0.9$ in Fig. 7(d), $\langle V\rangle = 0$ at small values of l_r, and as l_r increases $\langle V\rangle$ passes through a maximum value before decreasing again. In the larger l_r regime where $\langle V\rangle$ is a decreasing function of l_r, the drift velocity approximately follows the form $\langle V\rangle \propto 1/l_r$, as indicated by the dashed line fits in each panel.

In Fig. 8(a) we show the evolution of the three different phases as a function of F_D versus l_r for a system with $\phi_{\rm obs} = 0.1257$, $\phi_a = 0.03146$, and $F_m = 0.5$. In phase I, the ohmic flow regime, $\langle V\rangle$ increases with increasing F_D. In phase II, partial trapping occurs and we observe NDM. Phase III is the completely clogged regime with $\langle V\rangle = 0$. The extent of phase I grows as l_r increases until the I-II boundary saturates at large l_r to the value $F_D = 0.5$, corresponding to $F_D/F_m = 1.0$. Similar behavior appears for phase II, with a saturation of the II-III boundary for $l_r > 1$ to $F_D = 1.0$. The onset of phase III drops to $F_D = 0$ when $l_r = 0$, indicating that for this density, nonactive disks are permanently clogged. In Fig. 8(b) we plot a dynamic phase diagram as a function of F_D versus $\phi_{\rm tot}$, where we vary $\phi_{\rm tot}$ by fixing $\phi_{\rm obs} = 0.1257$ and changing ϕ_a. Phase III disappears for $\phi_{\rm tot} > 0.17$, and the extent of phase I increases as the ratio $\phi_a/\phi_{\rm obs}$ of active disks to obstacles increases.

3.1. Varied Obstacle Density and Motor Force

We next consider the effect of holding $\phi_{\rm tot}$ fixed at $\phi_{\rm tot} = 0.157$ while decreasing $\phi_{\rm obs}$. In Fig. 9(a) we plot $\langle V\rangle$ versus l_r for a sample with $\phi_{\rm obs} = 0.03146$. Here $\langle V\rangle$ decreases monotonically with increasing l_r and the flow persists even when $l_r = 0$. At $\phi_{\rm obs} = 0.0628$ in Fig. 9(b) and at $\phi_{\rm obs} = 0.09424$ in Fig. 9(c), there is still finite flow

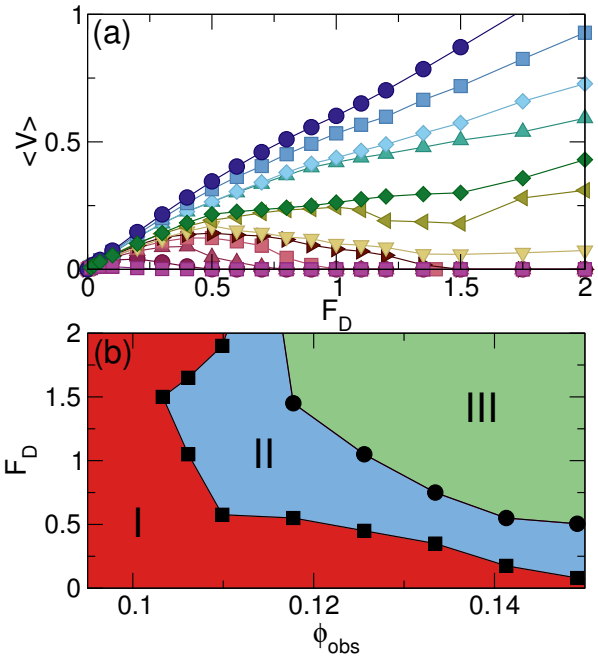

Figure 10. (a) $\langle V\rangle$ vs F_D for samples with fixed $\phi_{\rm tot} = 0.157$ and varied $\phi_{\rm obs}$ at $l_r = 1.0$ and $F_m = 0.5$. From top to bottom, $\phi_{\rm obs} = 0.00785$ (dark blue circles), 0.00864 (medium blue squares), 0.00942 (light blue diamonds), 0.102 (teal up triangles), 0.1033 (dark green diamonds), 0.10618 (light green left triangles), 0.1099 (yellow down triangles), 0.1178 (dark red right triangles), 0.1256 (light pink squares), 0.133 (dark pink up triangles), 0.1413 (dark magenta circles), and 0.149 (light magenta squares). (b) Dynamic phase diagram as a function of F_D vs $\phi_{\rm obs}$ for the system in panel (a), showing reentrance in phase I. Phase I (red): ohmic flow; phase II (blue): partial trapping with NDM; phase III (green): clogged.

for $l_r = 0$, and a peak in $\langle V\rangle$ emerges near $l_r = 1.0$. At $\phi_{\rm obs} = 0.1257$ in Fig. 9(d), $\langle V\rangle = 0$ when $l_r < 0.1$, and the optimum flow, indicated by the highest value of $\langle V\rangle$, has shifted to a higher run length of $l_r = 2.0$.

In Fig. 10(a) we plot $\langle V\rangle$ versus F_D for a system with $l_r = 1.0$, $F_m = 0.5$, fixed $\phi_{\rm tot} = 0.157$, and varied obstacle density ranging from $\phi_{\rm obs} = 0.007853$ to $\phi_{\rm obs} = 0.1492$. The upper value of F_D at which $\langle V\rangle$ drops to zero decreases with increasing $\phi_{\rm obs}$ for $\phi_{\rm obs} > 0.1178$, while for $0.1033 < \phi_{\rm obs} < 0.1178$ we observe a window of NDM where $\langle V\rangle$ decreases with increasing F_D separating low and high F_D regions in which $\langle V\rangle$ increases with increasing F_D. For $\phi_{\rm obs} < 0.1033$, $\langle V\rangle$ monotonically increases with increasing F_D, and although the NDM has disappeared, there is still a decrease in the slope of $\langle V\rangle$ for $F_D > 0.5$ because an increased amount of trapping occurs once $F_D > F_m$. Due to the harmonic form of the disk-disk interaction potential, if F_D is increased to a large enough value the disks eventually are able to depin and move even in the completely clogged state; however, this occurs well above the range of F_D that we consider here. In Fig. 10(b), the dynamic phase diagram as a function of F_D versus $\phi_{\rm obs}$ for the system in Fig. 10(a) shows that the ohmic flow phase I is reentrant.

Up to now we have characterized the activity by the run length $l_r = \tau F_m \delta t$

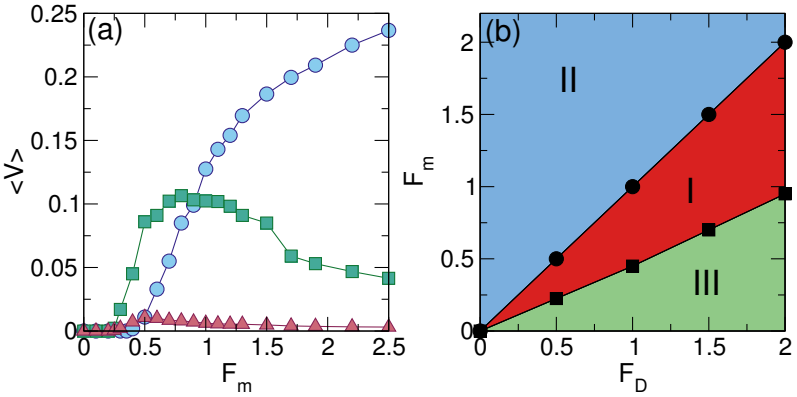

Figure 11. $\langle V \rangle$ vs the motor force F_m for a system with $F_D = 0.5$, $\phi_{\rm obs} = 0.1257$, and $\phi_a = 0.0314$ at $\tau = 100$ (circles), 10000 (squares), and 120000 (triangles). (b) Dynamic phase diagram as a function of F_m vs F_D for the same system at $\tau = 120000$.

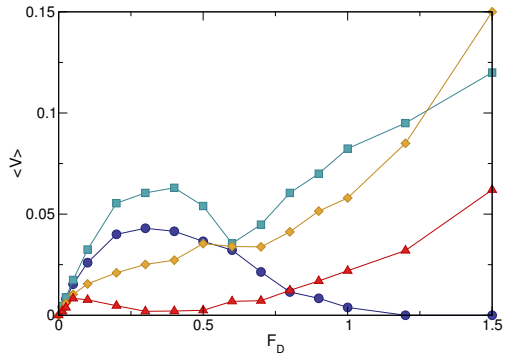

Figure 12. $\langle V \rangle$ vs F_D for samples with $\phi_{\rm obs} = 0.173$, $F_m = 0.5$, and $l_r = 1.0$ at $\phi_{\rm tot} = 0.25$ (blue circles), 0.377 (green squares), 0.565 (orange diamonds), and 0.7 (red triangles).

and have focused on the case $F_m = 0.5$. It is, however, possible to obtain different behaviors at fixed l_r by varying F_m and τ. If $F_D < F_m$, the value of $\langle V \rangle$ should always be finite. In Fig. 11(a) we plot $\langle V \rangle$ versus F_m in systems with fixed $F_D = 0.5$, $\phi_a = 0.0314$, and $\phi_{\rm obs} = 0.1257$ for three values of τ. In order to compare these plots to our previous results, note that for $F_m = 0.5$, $\tau = 100$ gives $l_r = 0.1$, $\tau = 10000$ is equivalent to $l_r = 10.0$, and $\tau = 120000$ corresponds to $l_r = 120$. For $\tau = 100$, $\langle V \rangle = 0$ when $F_m < 0.4$, and for $F_m \geq 0.4$, $\langle V \rangle$ increases monotonically with F_m. At $\tau = 10000$, $\langle V \rangle > 0$ for $F_m > 0.2$ and $\langle V \rangle$ passes through a maximum near $F_m = 0.8$. For $\tau = 120000$, the maximum in $\langle V \rangle$ falls at $F_m = 0.5$, and the overall magnitude of $\langle V \rangle$ is much smaller than that observed at the smaller τ values. In Fig. 11(b) we plot a dynamic phase diagram as a function of F_m versus F_D for the $\tau = 120000$ system. The I-III transition line separating the clogged phase III and the ohmic flow phase I falls at $F_m = F_D/2$, while the NDM in phase II appears when $F_m > F_D$.

In previous work examining the mobility as a function of ϕ_a for fixed $\phi_{\rm obs}$ and fixed F_D, $\langle V \rangle$ increased with increasing ϕ_a up to a maximum value and then decreased

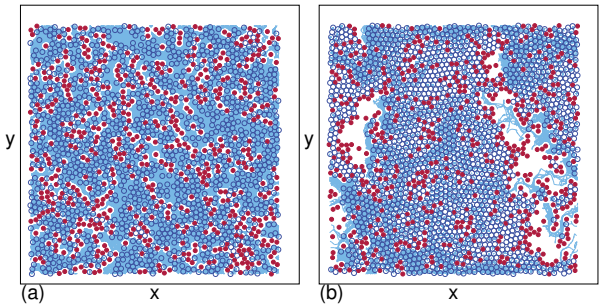

Figure 13. The obstacle positions (red filled circles), active disks (dark blue open circles), and trajectories (light blue lines) for the system in Fig. 12 at (a) $\phi_{\rm tot} = 0.565$ with $F_D = 0.0125$ and (b) $\phi_{\rm tot} = 0.7$ with $F_D = 0.5$.

for higher ϕ_a as the disks approached the jamming density due to a crowding effect in which the active disks become so dense that they impede each other's motion [10]. In Fig. 12 we plot $\langle V \rangle$ versus F_D for a system with $\phi_{\rm obs} = 0.173$, $F_m = 0.5$, and $l_r = 1.0$ at $\phi_{\rm tot} = 0.25$, 0.377, 0.565, and 0.7. For $\phi_{\rm tot} = 0.25$, $\langle V \rangle$ drops to zero for $F_D > 1.25$, while for $\phi_{\rm tot} = 0.377$, there is a region of NDM for $0.4 < F_D < 0.7$ but the velocities remain finite and the overall magnitude of $\langle V \rangle$ is larger than that of the $\phi_{\rm tot} = 0.25$ system. For $\phi_{\rm tot} = 0.565$, the average $\langle V \rangle$ is smaller than that at $\phi_{\rm tot} = 0.377$ due to the crowding effect, and there is only a very small window of NDM near $F_D = 0.6$. For $\phi_{\rm tot} = 0.7$, the increased crowding effect causes a substantial decrease in the overall magnitude of $\langle V \rangle$, and at the same time an extended region of NDM appears for $0.05 < F_D < 0.4$.

In Fig. 13(a) we plot the active disk trajectories for the system in Fig. 12 at $\phi_{\rm tot} = 0.565$ and $F_D = 0.0125$, a regime in which $\langle V \rangle$ increases with increasing F_D. There is a considerable amount of disk motion throughout the system. In contrast, Fig. 12(b) illustrates an NDM regime at $\phi_{\rm tot} = 0.7$ and $F_D = 0.5$, where a large jammed or clogged area has formed in the center of the sample, indicating the role played by crowding in inhibiting the mobility of the active disks.

4. Summary

We have numerically examined the velocity-force curves for active matter disks driven through a random obstacle array and find three distinct dynamical phases. In the low drive regime, the velocity increases linearly with increasing external drive. For intermediate drives, the system exhibits negative differential mobility where the velocity decreases with increasing drive due to the trapping of disks behind obstacles. Finally, at high drive we find a fully clogged state in which the drift velocity drops to zero. For increasing activity or run length, we find that the onsets of the NDM phase and the fully clogged phase are shifted to larger external drift forces. Additionally, the drift velocity at fixed drive changes nonmonotonically with increasing activity, indicating that there is a drive-dependent optimal activity or run length that maximizes the flux of disks through the system. We map the locations of the dynamic phases as a function of activity, active disk density, obstacle density, and motor force. We describe how an external drift force could be tuned to either separate or mix active disk species with different mobilities. We have also examined the role of

active disk density, and find that at low disk densities, the NDM and clogging effects disappear with increasing disk density when the trapping is reduced; however, for much larger densities where crowding effects become important, the NDM reappears and is enhanced.

Acknowledgments

This work was carried out under the auspices of the NNSA of the U.S. DoE at LANL under Contract No. DE-AC52-06NA25396.

References

[1] Marchetti M C, Joanny J F, Ramaswamy S, Liverpool T B, Prost J, Rao M and Simha R A 2013 Hydrodynamics of soft active matter *Rev. Mod. Phys.* **85** 1143
[2] Bechinger C, Di Leonardo R, Löwen H, Reichhardt C, Volpe G and Volpe G 2016 Active Brownian particles in complex and crowded environments *Rev. Mod. Phys.* **88** 045006
[3] Reichhardt C and Reichhardt C J O 2015 Active microrheology in active matter systems: Mobility, intermittency, and avalanches *Phys. Rev. E* **91** 032313
[4] Fily Y and Marchetti M C 2012 Athermal phase separation of self-propelled particles with no alignment *Phys. Rev. Lett.* **108** 235702
[5] Redner G S, Hagan M F and Baskaran A 2013 Structure and dynamics of a phase-separating active colloidal fluid *Phys. Rev. Lett.* **110** 055701
[6] Palacci J, Sacanna S, Steinberg A P, Pine D J and Chaikin P M 2013 Living crystals of light-activated colloidal surfers *Science* **339** 936
[7] Cates M E and Tailleur J 2013 When are active Brownian particles and run-and-tumble particles equivalent? Consequences for motility-induced phase separation *Europhys. Lett.* **101** 20010
[8] Cates M E and Tailleur J 2015 Motility-induced phase separation *Annu. Rev. Condens. Mat. Phys.* **6** 219
[9] Thompson A G, Tailleur J, Cates M E and Blythe R A 2011 Lattice models of nonequilibrium bacterial dynamics *J. Stat. Mech.* **2011** P02029
[10] Reichhardt C and Reichhardt C J O 2014 Active matter transport and jamming on disordered landscapes *Phys. Rev. E* **90** 012701
[11] Morin A, Desreumaux N, Caussin J-B and Bartolo D 2017 Distortion and destruction of colloidal flocks in disordered environments *Nature Phys.* **13** 63
[12] Zeitz M, Wolff K and Stark H 2017 Active Brownian particles moving in a random Lorentz gas *Eur. Phys. J. E* **40** 23
[13] Lozano C, ten Hagen B, Löwen H and Bechinger C 2016 Phototaxis of synthetic microswimmers in optical landscapes *Nature Commun.* **7** 12828
[14] Sándor Cs, Libál A, Reichhardt C and Reichhardt C J O 2017 Collective transport for active matter run-and-tumble disk systems on a traveling-wave substrate *Phys. Rev. E* **95** 012607
[15] Choudhury U, Straube A V, Fischer P, Gibbs J G and Höfling F 2017 Active colloidal propulsion over a crystalline surface *Preprint* arXiv:1707.05891
[16] Pince E, Velu S K P, Callegari A, Elahi P, Gigan S, Volpe G and Volpe G 2016 Disorder-mediated crowd control in an active matter system *Nature Commun.* **7** 10907
[17] Sándor Cs, Libál A, Reichhardt C and Reichhardt C J O 2017 Dynamic phases of active matter systems with quenched disorder *Phys. Rev. E* **95** 032606
[18] Reichhardt C J O and Reichhardt C 2017 Ratchet effects in active matter systems *Annu. Rev. Condens. Mat. Phys.* **8**, 51
[19] Kümmel F, Shabestari P, Lozano C, Volpe G and Bechinger C 2015 Formation, compression and surface melting of colloidal clusters by active particles *Soft Matter* **11** 6187
[20] Chepizhko O, Altmann E G and Peruani F 2013 Optimal noise maximizes collective motion in heterogeneous media *Phys. Rev. Lett.* **110** 238101
[21] Quint D and Gopinathan A 2015 Topologically induced swarming phase transition on a 2D percolated lattice *Phys. Biol.* **12** 046008
[22] Reichhardt C and Reichhardt C J O 2017 Depinning and nonequilibrium dynamic phases of particle assemblies driven over random and ordered substrates: A review *Rep. Prog. Phys.* **80** 026501
[23] Barma M and Dhar D 1983 Directed diffusion in a percolation network *J. Phys. C* **16** 1451

[24] Leitmann S and Franosch T 2013 Nonlinear response in the driven lattice Lorentz gas *Phys. Rev. Lett.* **111** 190603
[25] Baerts P, Basu U, Maes C and Safaverdi S 2013 Frenetic origin of negative differential response *Phys. Rev. E* **88** 052109
[26] Bénichou O, Illien P, Oshanin G, Sarracino A and Voituriez R 2014 Microscopic theory for negative differential mobility in crowded environments *Phys. Rev. Lett.* **113** 268002
[27] Baiesi M, Stella A L and Vanderzande C 2015 Role of trapping and crowding as sources of negative differential mobility *Phys. Rev. E* **92** 042121
[28] Bénichou O, Illien P, Oshanin G, Sarracino A and Voituriez R 2016 Nonlinear response and emerging nonequilibrium microstructures for biased diffusion in confined crowded environments *Phys. Rev. E* **93** 032128
[29] Sarracino A, Cecconi F, Puglisi A and Vulpiani A 2016 Nonlinear response of inertial tracers in steady laminar flows: differential and absolute negative mobility *Phys. Rev. Lett.* **117** 174501
[30] Jack R L, Kelsey D, Garrahan J P and Chandler D 2008 Negative differential mobility of weakly driven particles in models of glass formers *Phys. Rev. E* **78** 011506
[31] Reichhardt C, Olson C J and Nori F 1998 Nonequilibrium dynamic phases and plastic flow of driven vortex lattices in superconductors with periodic arrays of pinning sites *Phys. Rev. B* **58** 6534
[32] Gutierrez J, Silhanek A, Van de Vondel J, Gillijns W and Moshchalkov V 2009 Transition from turbulent to nearly laminar vortex flow in superconductors with periodic pinning *Phys. Rev. B* **80** 140514
[33] Eichhorn R, Regtmeier J, Anselmetti D and Reimann P 2010 Negative mobility and sorting of colloidal particles *Soft Matter* **6** 1858
[34] Scholl E 1987 *Nonequilibrium Phase Transitions in Semiconductors* (Berlin:Springer-Verlag)